Combination of molecular beam sampling and laser-based techniques for studies of flame-assisted material synthesis: the case of Iron Oxide

M. Poliak[1], A. Fomin[1], V. Tsionsky[1], S. Cheskis[1], I. Wlokas[2] and I. Rahinov[*,3]

[1]School of Chemistry, Tel Aviv University, Tel Aviv 69978, Israel
[2]Institute for Combustion and Gas dynamics - Fluid Dynamics, University of Duisburg-Essen, 47057 Duisburg, Germany
[3]Department of Natural Sciences, The Open University of Israel, Raanana 4353701, Israel

Abstract

The current work is aimed towards a comprehensive elucidation of the mechanism governing metal oxide nanoparticles (NPs) synthesis in flame-reactors. Those make up a versatile and easily scalable environment, however, due to the harsh flame conditions, *in-situ* diagnostics, which in the current case are of surmount importance, become increasingly challenging. Below, we describe the diagnostic tools at our disposal, which comprise of both molecular beam sampling (Particle-Mass-Spectrometry-Quartz-Crystal-Microbalance, LID-QCM) and laser-based (Intra-Cavity-Laser-Absorption-Spectroscopy) techniques, their application on the case study of iron oxide NPs and their implications on the possible mechanism of metal oxide NPs formation in flames.

Introduction

Flame-assisted synthesis offers a convenient route for production of nano-shaped metal oxide materials. Detailed understanding of the mechanism governing the particle formation in flames, based on the input gained from detailed measurements, is a necessary pre-requisite for flame synthesis of NPs with tailored functionalities, which can then be used in diverse applications such as: magnetic resonance imaging, heterogeneous catalysis, targeted drug delivery etc. (see for instance review by Lu et al. [1] and references therein). However, the high-temperature particle–laden environment imposes considerable challenges on in-situ diagnostics and methods addressing both solid and gas phase products and intermediates are required. In this work, focused on the flame assisted synthesis of iron oxide nanoparticles we have applied combination of molecular beam sampling and laser-based methods. Specifically, low pressure, premixed, laminar flat flame of CH_4/O_2, doped with iron pentacarbonyl was studied using several methods: (1) a combined quartz-crystal-microbalance-particle-mass-spectrometry (QCM-PMS) [2]; (2) laser-induced quartz-crystal microbalance (LID-QCM) detuning [3] and (3) intracavity laser absorption spectroscopy (ICLAS) [4] techniques. The application of ICLAS, which is insensitive to the broadband losses induced by light scattering on solid particulates we were able to map the distribution of gas-phase FeO in heavily particle laden environment, where the sensitivity of techniques traditionally applied for laser-based combustion diagnostics (e.g. LIF and CRDS) is hampered. The newly-developed LID-QCM technique paves the way towards *quasi-in-situ* optical characterization of as-sampled flame synthesized nanoparticles.

By studying the mass concentration and particle size distribution with QCM-PMS, we have unambiguously demonstrated, that the formation of nanoparticles in iron pentacarbonyl-doped flames occurs very early, in close proximity to the burner surface, prior to the flame front. This early rise of nanoparticle mass concentration is followed by a sharp drop in the nanoparticle concentration at the high temperature flame front. This "prompt" nanoparticle generation is consistent with kinetic models describing iron cluster formation. This observation presents a challenge and a trigger for further development of the existing mechanisms for gas phase synthesis of iron oxide particles in flames.

Experimental setup

A detailed description of the PMS-QCM apparatus is found elsewhere [2-3, 5], so only a brief account will be presented here. The schematic of the experimental setup is depicted in Fig. 1.

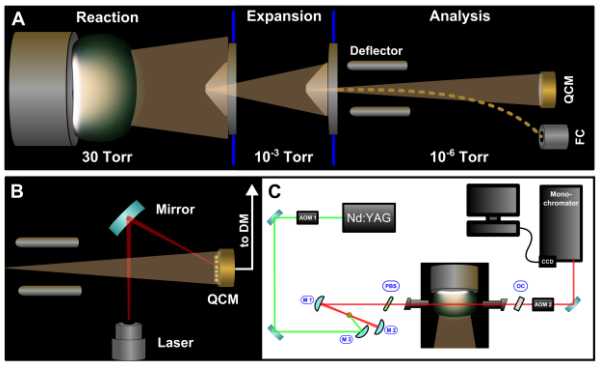

Figure 1 – (A) Schematic of PMS-QCM. Gases are delivered via mass flow controllers to the burner located in the flame synthesis reactor. The gases then expand supersonically via the sampling orifice to the expansion chamber. The central part of the jet is skimmed prior to

Corresponding author: igorra@openu.ac.il

entering the analysis chamber. Upon passing the deflector, charged particles are shifted and reach the Faraday Cup (FC), while neutral particles are collected directly below on the QCM (B) Experimental setup used for optical characterization of NPs deposited on the QCM (C) Setup for ICLAS measurements in a nanoparticle flame reactor. The pumping laser beam (frequency doubled output of an Nd–YAG laser) is focused on the dye jet by mirror M3. The homebuilt dye laser cavity is formed by mirrors M1, M2 and OC (output coupler). AOM1 and AOM2 are acousto-optic modulators. CCD—is a charge coupled device. PBS—is a pellicle beam splitter.

Two burner systems (situated in the reactor chamber, see Fig.1A) for generating low-pressure $CH_4/O_2/N_2$ flames were deployed. In a low-pressure system the flame front is wide enough to sample concentration profiles of gas-phase molecules and radicals as well as nascent nanoparticles with sufficient resolution required to recover detailed kinetic information. One such system is a flat flame porous plug McKenna burner producing a flat premixed quasi-one-dimensional flame. The quasi-1D structure of this flame facilitates diagnostics and generating data most readily comparable to theoretical models. To extend the range of operating conditions and ease the access to the flame front, a modified hybrid McKenna burner equipped with a narrow central tube was employed. The analysis protocol of PMS-QCM (Fig. 1A) technique includes molecular beam sampling, sorting the charged particles constituent according to mass/charge ratio (*m/ze*) via electrostatic deflection [2], and detection of neutral particles by monitoring the variation of the quartz crystal oscillation frequency upon exposure to the particle-laden molecular beam [6]. The particle charge is mostly unity for the relevant range of particle sizes. The particle velocity is measured independently with the aid of electrostatic chopper located downstream of the mass-selecting capacitor. This methodology allows direct in-situ determination of the total particle mass concentration and probability density distribution of *m/ze*. From these quantities particle number concentration in the flame aerosol can be determined.

LID-QCM technique (Fig 1B): The PMS-QCM apparatus previously described was modified by the incorporation of a periodically applied He-Ne laser beam (633 nm) penetrating a window in the analysis chamber and deflected by a mirror such, that it irradiated the QCM (see Fig. 1B). PMS was not in use during these experiments. The magnitude of the frequency detuning of the quartz crystal is proportional to the energy absorbed on one of the quartz crystal electrodes and once NPs are deposited on the crystal, the magnitude of the detuning reflects the magnitude of the absorption coefficient of the NPs.

ICLAS (Fig 1C) is a method in which absorbing species are placed inside the cavity of a broadband laser. Due to the positive feedback mechanism in lasers, even minute quantities of a narrow-line absorber will produce holes in the spectrum where the laser output is partially quenched. The reaction chamber used in our previous experiments is placed inside the cavity of a homebuilt quasi-cw dye-jet laser and is isolated from other parts of the cavity by two glass windows placed at Brewster's angle. The laser consists of the dye jet placed inside an astigmatically compensated, three-mirror folded cavity formed by M1, M2 and OC (output coupler). The central wavelength of this broadband laser source can be tuned by introducing a thin pellicle beamsplitter inside the cavity. The laser generation time t_g, in the ICLAS is the time interval between the beginning of the laser generation and the sampling, which is controlled with the aid of two acousto-optical modulators (AOM1 and AOM2). The spectral output is analyzed with the aid of a high resolution spectrograph. ICLAS is not sensitive to the broadband absorption by the NPs, allowing to monitor FeO in a particle-laden environment. The OH The OH spectra (R-branch of the (0,0) band of the $A^2\Sigma+-X^2\Pi i$ system centered around 307 nm) were measured by laser induced fluorescence (LIF) and used for the evaluation of temperature profiles of flame gases according to protocol described elsewhere [7]

In some experiments the LIF laser access optical ports were equipped with high reflectivity concave mirrors to conduct cavity ring down spectroscopy (CRDS) measurements near 307 nm.

Results and Discussion

Mass concentration and particle mass variation

Fig.2 presents the QCM signal vs. the distance from the burner (DFB) recorded in fuel rich, hybrid, bulb shaped flame doped with $Fe(CO)_5$. The QCM signal, that is the rate of the quartz crystal frequency variation, is proportional to the mass flux of deposited nanoparticles.

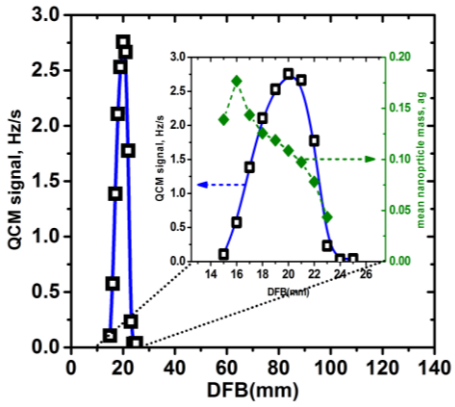

Figure 2 – Dependence of the QCM signal on the DFB for the hybrid, bulb-shaped burner configuration. Insert: zoom on the 14-26 mm DFB range (left y-axis) and the variation of the mean NP mass in that range.

Since the efficiency of the molecular beam sampling is not affected substantially by the flame conditions the QCM deposition rate profiles, are, in fact mass concentration profiles in relative units. This flame exhibits strong luminosity in relatively narrow region in the vicinity of the flame front originating from blackbody

radiation of hot, nascent nanoparticles. Consistent with this observation, the nanoparticle mass concentration increases sharply prior to the flame front (reaching a maximum at DFB~20 mm) and then drops abruptly ~ 5 mm downstream. The QCM measurements at each DFB were synchronized with measurements of PMS current dependence on the deflection voltage, allowing to derive the *m/ze* probability density distribution. From these data, within the reasonable assumption of singly-charged particles [8], nanoparticle mean mass was derived and shown to exhibit ~4-fold decrease across the ~ 5mm of the mass concentration peak in the vicinity of the flame front. The sharp drop of the nanoparticle mass concentration past the flame front is very peculiar, since the existing mechanisms of NPs formation predicted monotonic growth of the total mass concentration of iron oxide NPs with the increase of the reaction coordinate along with growth of the NP diameter. For the case of the bulb-shaped flame this sharp drop can result both from the evaporation/oxidation of the nascent nanoparticles in the high temperature and radical-rich flame front as well as from particles traveling along diverging (radial) trajectories originating from the curved front of the bulb-shaped flame. However, line-of-sight CRDS measurements (depicted in Fig. 3) exhibit qualitatively a similar trend: the ring-down decay (due to off-resonance scattering of NPs) coefficient peaks sharply in the vicinity of the burner surface followed by a steep decrease.

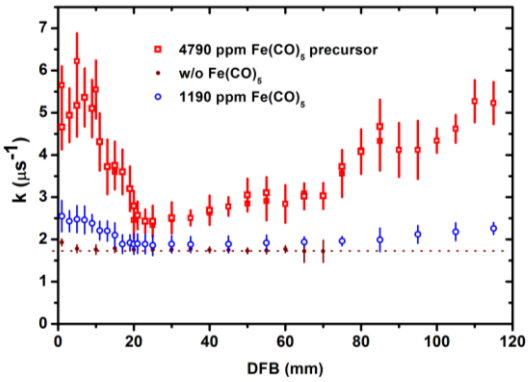

Figure 3 – CRDS measurements, ring-down decay coefficient vs DFB without added precursor (black dots), with a 1190 ppm concentration of precursor (blue circles) and with a 4790 ppm concentration of precursor (red squares).

At higher DFBs a gradual decrease of the decay coefficient is observed. It's worth noting, that one must be cautious when making a direct comparison since: QCM is a point measurement technique while CRDS is a line-of-sight one; CRDS is not intrusive, while in the case of QCM the probe can shift the flame temperature distribution, and therefore, the gas and solid particulates profiles. Nevertheless, the observation of the sharp drop in the CRDS coefficient profile cannot be explained by divergence of the nascent particles, since those would be detected due to the line-of-sight nature of the method. These findings strongly suggest that a destruction process (evaporation/ oxidation) is taking place at the high temperature flame front. At DFBs larger than 60 mm the decay coefficient grows monotonically, indicating the reappearance of solid particulates.

To further investigate this phenomenon experiments with a quasi-1-dimentional flat flame were conducted allowing for direct comparison of species concentration measurements and kinetic models output (Fig. 4). A similar sharp decrease of the nanoparticle mass concentration is observed for the flat flame configuration. This observation and the steep decrease of the particle mass across the narrow region of the flame front suggest that particle oxidation/decomposition is a more favorable reason for the abrupt drop of the particle mass concentration.

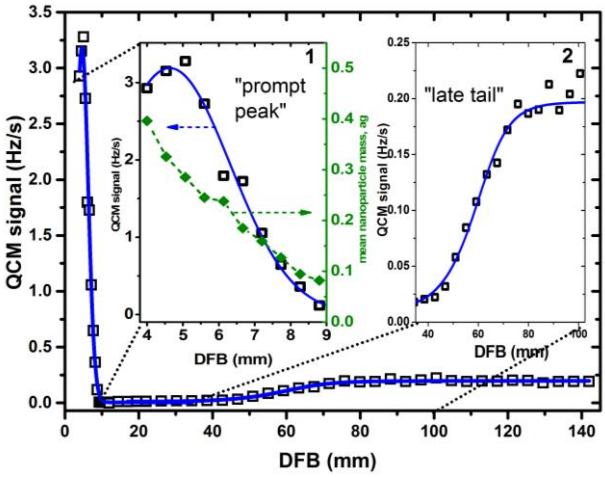

Figure 4 – Dependence of the QCM signal on DFB for the flat quasi-1-D flame. Inserts: (1) zoom on the 4-9 mm DFB range (left y-axis) and the variation of the mean NP mass in that range; (2) zoom on the 37-100 mm DFB range (left y-axis) and the variation of the mean NP mass in that range.

This observation can be rationalized within the following line of thought: when the $Fe(CO)_5$ concentration is sufficient its decomposition produces enough Fe atoms to give rise to the nucleation process in the vicinity of the burner surface. As the temperature increases towards the flame front (where it reaches ~1700K) the nascent NPs return to the gas phase via evaporation and oxidation processes. This is consistent with the decrease in particle size and mass concentration. With the decrease of the temperature at large distances from the burner surface, the particles reappear producing the "late tail". The different magnitudes of the "prompt" peak and "late tail" can be attributed to thermos-phoretic particle redistribution and gas composition dependence of the nucleation process. Within the vicinity of the burner surface, the nucleation of the iron atoms to clusters competes with gas phase reactions such as oxidation. Therefore, sufficient precursor concentration would be required for inception of the nucleation process. Indeed, the experiment shows that the dependence of nanoparticle mass concentration on the concentration of the $Fe(CO)_5$ dopant exhibits threshold-like behavior.

This can be described by a simplistic, two reactions model:

(1) $Fe + Fe \overset{k_1}{\Rightarrow} nanoparticles$

(2) $Fe \overset{k_2}{\Rightarrow} gas\ phase\ products$

Under the assumption that all iron atoms generated via the $Fe(CO)_5$ decomposition yield nanoparticles with the exception of those that are converted to gaseous products, simple kinetic consideration lead to the following dependence of nanoparticle mass concentration, m_{NP}, on the initial amount of $Fe(CO)_5$ precursor [5]:

(3) $$m_{NP} = M_{Fe}[N_{Fe(CO)_5} - \left(\frac{k_1}{k_2}\right) \ln\left(N_{Fe(CO)_5}\frac{k_1}{k_2} + 1\right)]$$

Where M_{Fe} is the mass of the iron atom and $N_{Fe(CO)_5}$ is the initial concentration of iron pentacarbonyl. Eq. (3) captures well the observed dependence of nanoparticle mass concentration on the precursor load as can be seen upon the inspection of Fig. 5. These findings were further investigated with the application of a 1-D numerical simulation. The mechanism used for the numerical 1-D simulation, is compiled from three sources. The CH_4/O_2 system is described by the GRI3.0 mechanism [9], while the thermal decomposition of $Fe(CO)_5$ and the formation of $Fe_{2<n<8}$ clusters were simulated using the mechanism proposed by Wen et al. [10]. The interplay of iron containing species with hydrocarbon flame chemistry and the formation of iron oxide was described using a modified and extended mechanism of Rumminger et al. [11] and Wlokas et al. [12]. The 1-D simulation of the flat laminar synthesis flame was conducted using the reaction kinetics library Cantera [13]. The flame temperature profile measured by the OH-LIF technique was used as input for the simulation to effectively account for heat losses in the reactor. Simulation results were compared to experimental data and those obtained from the simplistic model mentioned above (Fig. 5). Both the simplistic model and the simulation based on a detailed mechanism capture well the experimentally observed trend.

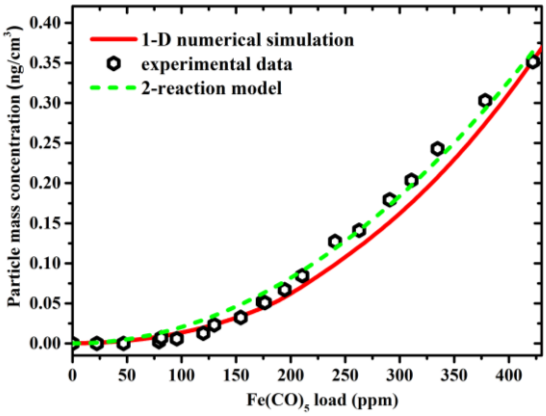

Figure 5 - Dependence of NP mass concentration, measured at DFB=8 mm on the load of the $Fe(CO)_5$ precursor in the unburned, premixed gases. Empty hexagons - QCM measured experimental data (normalized to the value of mass concentration predicted by numerical simulation at the highest precursor load). Red solid line - prediction based on a numerical simulation using a detailed reaction mechanism [12]. Green dashed line - behavior predicted by the simple analytical model based on 2 reactions (see text).

While the experiments conducted in the flat flame strengthen the hypothesis of early metallic particle formation, it would be interesting to explore the range of conditions where this process partakes a significant role. This would include working under a wide range of fuel/oxidant ratios, gas flows and precursor concentrations. Unfortunately, expanding the range of operating conditions is limited for a premixed flat flame due to flammability limits. For this goal, the hybrid 2-stage flame allowing for a wide range of operating conditions can be utilized. This is possible due to the stabilizing effect of the primary flame serving as the source of energy to the central, secondary flame therefore allowing for a wide range of operating conditions. Our preliminary results in this direction are shown in Fig. 6. We have found, that by increasing the total gas flow rate in the central flame without varying the fuel/oxidant ratio, it possible to break down the regime of early particle formation.

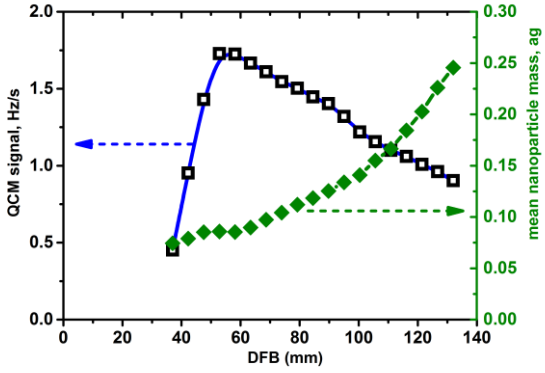

Figure 6 - Dependence of the QCM signal on the DFB for the hybrid, bulb-shaped burner configuration for a DFB range 37-140 mm (left y-axis) and the variation of the mean NP mass in that range (right y-axis).

The measurements exhibited in Fig. 6 were conducted when the total flowrate of the gases in the central flame was increased by a factor of 3.5. This flame exhibits an extended particle luminosity zone, starting at relatively large distances from the burner (above 40 mm). Consistent with this observation a strong QCM signal is observed for DFB>40 mm. The decrease of the QCM signal at DFBs above 60 mm is probably related to particle divergence as well as different nucleation conditions. Note, that mean NP mass exhibits a monotonic growth as the DFB increases. A more detailed analysis of the kinetic fingerprints obtained in these 3D hybrid flames, would require a more elaborate computational fluid dynamics calculations. These efforts are currently underway in our laboratory.

Optical characterization of as-deposited nanoparticles

While the combination of QCM with PMS allows to evaluate the mass concentration, *m/ze* distribution and number concentration of nascent nanoparticles it doesn't provide diagnostics of their optical properties. Here we exploited the phenomenon of QCM frequency detuning upon interaction with light. Our observations indicate that irradiation of the quartz crystal leads to a significant increase of the QCM resonance frequency even for relatively low intensities (in the order of mW) -see Fig.7A.

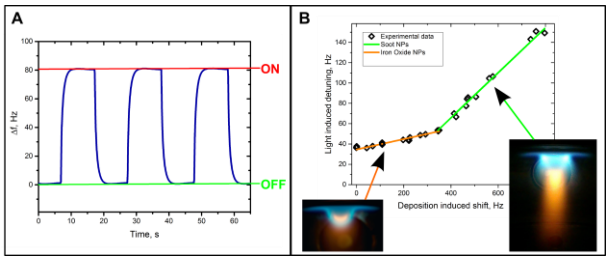

Figure 7 - (A) Modulation of the QCM (6 MHz gold coated quartz crystal) frequency induced by the modulation of laser irradiation. Laser radiation is switched on/off every 10 s. Laser power is 35.6 mW, laser wavelength is 532 nm (B) The dependence of the laser-induced detuning on the mass of the NP deposit(expressed via the baseline frequency decrease) for iron oxide and soot NPs. The deposition of soot NPs started after the deposition of iron oxide NPs on the same QCM; insert: The shift of the QCM frequency upon irradiation by 633 nm laser during the NP deposition. The dashed line shows the baseline variation of the QCM crystal frequency induced by the mass growth resulting from NP deposition.

The dependence of the magnitude of the observed light–induced detuning (LID) phenomenon the pressure and heat conductivity of the surrounding gas and its linear dependence on the laser intensity suggests that it originates from thermally induced stress of the quartz crystal [3]. Therefore, the magnitude of the frequency detuning effect is proportional to the amount of energy absorbed on one of the crystal electrodes. When the crystal is covered by flame-generated nanoparticles, the amount of the laser energy absorbed, and the consequent frequency detuning reflect the magnitude of the absorption coefficient of the NP layer. In Fig. 7B, we compare the effect of light-induced detuning for two types of nanoparticles: iron oxide and soot particles obtained in an acetylene flame with a C/O ratio of 2.5. During nanoparticle deposition on the QCM the resonance frequency decreases linearly due to the accumulation of the deposited mass. Fig. 3B depicts the dependence of the frequency jumps magnitudes on the shift of the baseline resonance frequency, which is proportional to the amount of the deposited material (4.26 μg/cm^2 of iron oxide nanoparticles followed by 5.49 μg/cm^2 of soot). The slope of the dependence shown in Fig. 3B is a mass-normalized quantity, directly correlating with the absorption coefficient of the nanoparticle deposit: indeed, the slope is four times higher for soot compared to iron oxide NPs, consistent with a higher absorption coefficient of soot at the He–Ne wavelength.

Monitoring of gas phase species in a particle laden environment: FeO

Quantitative *in-situ* measurements of the concentration of gas-phase iron-containing species are required for further development and validation of chemical mechanisms governing the precursor decomposition and particle formation. Flames doped with $Fe(CO)_5$ are sensitive to the presence of iron containing species [14], and, in particular, FeO is intimately related to the fire-suppressing properties of iron-containing compounds, as it reacts in a catalytic cycle with flame carrier radicals and atoms (H and OH). We have monitored FeO by ICLAS in the 611-nm band range [4]. Despite the considerable body of studies devoted to spectroscopic detection of FeO the work of McMillin et al [15] is perhaps the only one where laser based detection and semi-quantitatively spatial distributions of FeO in the NP flame reactor were reported. However, the sensitivity of the LIF technique used in [15] is considerably hampered due to a broadband background originating from increased flame luminosity and laser light scattering interferences. This disadvantage can be circumvented by the utilization of ICLAS where the laser gain compensates broadband cavity losses due to light scattering on solid particulates present in the nanoparticle synthesis reactor. The FeO spectrum shown in Fig. 8 was recorded in a flame doped with 545 ppm of $Fe(CO)_5$ precursor. A signal-to-noise ratio as high as 30 is observed under our experimental conditions. Since we found the iron oxide absorbance signal to be linearly dependent on the amount of precursor, it implies that FeO would be detectable for $Fe(CO)_5$ precursor concentrations as low as 20 ppm. Sensitivity can be further increased by increasing the effective pathlength in the ICLAS experiment. This can be accomplished by either increasing the filling ratio of the cavity (only 2/90 under our conditions) or by increasing the generation time.

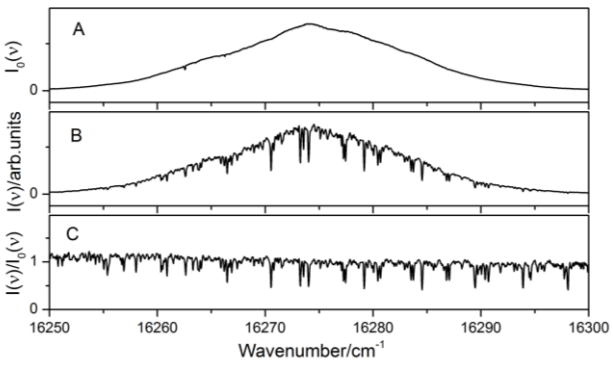

Figure 8 – (A) Dye-jet laser generation spectral profile, recorded for various positions of the pellicle

beam splitter at ~13 mm from the burner in the fuel-rich $CH_4/O_2/N_2$ flame without iron pentacarbonyl; (B) dye-jet laser generation spectral profile, recorded for various positions of the pellicle beam splitter at ~13 mm from the burner in the fuel-rich $CH_4/O_2/N_2$ flame after the addition of 545 ppm of iron pentacarbonyl; (C) normalized ICLAS spectrum (B/A) containing features originating from the addition of $Fe(CO)_2$.

Conclusions

In this work we have exploited several techniques combining molecular beam probing, mass spectrometry quartz crystal microbalance and laser based diagnostics to address various aspects of iron oxide nanoparticles formation in flames doped with iron pentacarbonyl. PMS-QCM measurements reveal that nanoparticles can form very early, prior to the flame front. This early formation followed by an abrupt drop of particle mass concentration in the flame front can be rationalized (at least semi-quantitatively) within a framework of a model incorporating early clustering of iron atoms produced by decomposition of $Fe(CO)_5$ precursor. The steep disappearance of the particles past the flame front can be attributed to evaporation and oxidation at the high temperature and radical rich flame front, rather than particle travel along diverging trajectories as was demonstrated by the comparison to CRDS. As the gases cool down further downstream the particles reappear, albeit exhibiting a weaker QCM signal (and larger mean NP masses). Proof-of-principle demonstration of the LID-QCM technique was described, highlighting its potential for measuring the absorption spectra of as deposited nanoparticles. ICLAS was shown to be a compelling method for high sensitivity monitoring of FeO in reacting particle laden environment. We hope that this work will stimulate further kinetic modeling to better understand flame-assisted nanoparticle synthesis.

Acknowledgements

This work was supported in part by the Israel Science Foundation (Grant No. 1149/12), Israel Ministry of Energy and Water Resources (Grant No. 211-11-007/2011-7-10) and the Research Authority of The Open University of Israel (GrantNo. 47324).

References

1. H. Lu, E.L. Salabas, F. Schüth,, *Angew. Chem. (Int. ed.)* **46,** 1222–1244 (2007)

2. A. Fomin, M. Poliak, I. Rahinov, V. Tsionsky and S. Cheskis, *Combust. Flame* **160**, 2131 – 214 (2013)

3. A. Fomin, M. Poliak, V. Tsionsky, S. Cheskis, I. Rahinov, *Sensors and Actuators B* **202**, 861–865 (2014)

4. I. Rahinov, A. Fomin, M. Poliak, S. Cheskis, *Appl. Phys. B,* **117(1),** 317-323 (2014)

5. M. Poliak, A. Fomin, V. Tsionsky, S. Cheskis, I. Wlokas and I. Rahinov, *Phys. Chem. Chem. Phys*., **17(1)**, 680-685 (2015)

6. A. Hevroni, H. Golan, A. Fialkov, I. Rahinov, V. Tsionsky, G. Markovich and S. Cheskis, *Measurement Science & Technology*, **22,** 115 (2011)

7. I. Rahinov, A. Goldman and S. Cheskis, *Combust. Flame*, 145, 105–116 (2006)

8. C. Janzen, P. Roth, *Combust. Flame* **125**, 1150–1161 (2001)

9. C.Bowman, R.Hanson, D.Davidson, W.Gardiner, V.Lissianski, G.Smith, D.Golden, M.Frenklach, H.Wangand, M.Goldenberg, GRI mechanism ver 3.0 see http://www.me/berkeley.edu/gri mech, 1997.

10. J. Z. Wen, H. Richter, W. H. Green, J. B. Howard, M. Treska, P. M. Jardim and J. B. Vander Sande, *Journal of Materials Chemistry*, **18**, 1561 (2008)

11. M. Rumminger and G. Linteris, *Combust. Flame*, **128**, 145–164 (2002)

12. I. Wlokas, A. Faccinetto, B. Tribalet, C. Schulz and A. Kempf, *Int. J. Chem. Kinet*., **45**, 487–498 (2013)

13. D. Goodwin, N. Malaya and H. S. R. Moffat

14. M.D. Rumminger, D. Reinelt, V. Babushok, G.T. Linteris, *Combust. Flame* **116(1–2),** 207 (1999)

15. B.McMillin, P.Biswasand M.Zachariah, *J.Mater.Res*., **11**,1552– 1561 (1996)